

Supplementary Materials for

Tunable intraband optical conductivity and polarization-dependent epsilon-near-zero behavior in black phosphorus

Souvik Biswas, William S. Whitney, Meir Y. Grajower, Kenji Watanabe, Takashi Taniguchi, Hans A. Bechtel, George R. Rossman, Harry A. Atwater*

*Corresponding author. Email: haa@caltech.edu

Published 8 January 2021, *Sci. Adv.* 7, eabd4623 (2021)
DOI: 10.1126/sciadv.abd4623

This PDF file includes:

Figs. S1 to S14
Table S1
References

BP band-edge and subband spectrum:

To display the band-edge and the higher subband regime for BP with better clarity, we take advantage of the known lack of optical response in BP along the ZZ direction and present the differential change in reflectance in Fig. S1, calculated as $\frac{\Delta R}{R} = \frac{\frac{R_{AC}}{R_{Au}} - \frac{R_{ZZ}}{R_{Au}}}{\frac{R_{ZZ}}{R_{Au}}}$. In this case the ZZ direction acts as a dielectric

background and one can see a very strong dip associated with the band edge (optical gap) which is convoluted with a reflectance dip associated with optical interference in the complete heterostructure. Weaker but clear spectral variations are also visible, coming from the higher subbands.

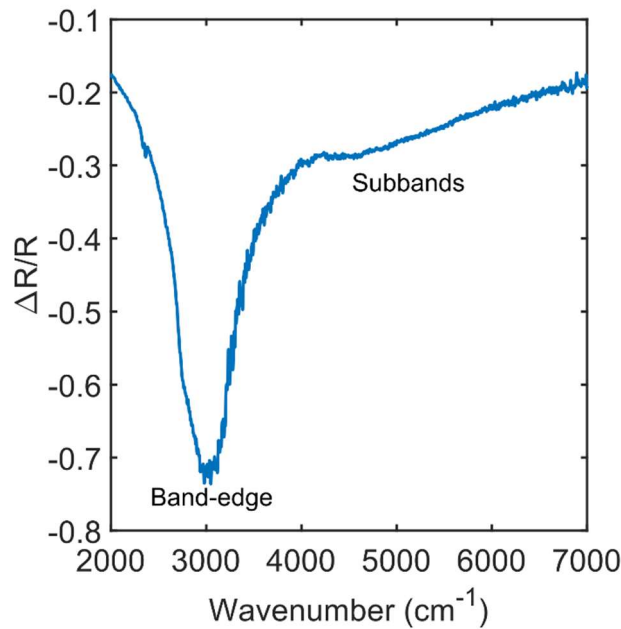


Fig. S1. Differential reflectance change in BP. The band-edge is convoluted with the interference dip.

Characterization of the crystal axes:

Polarized Raman measurements were performed shown in Fig. S2, to identify the AC and ZZ axis in our device.

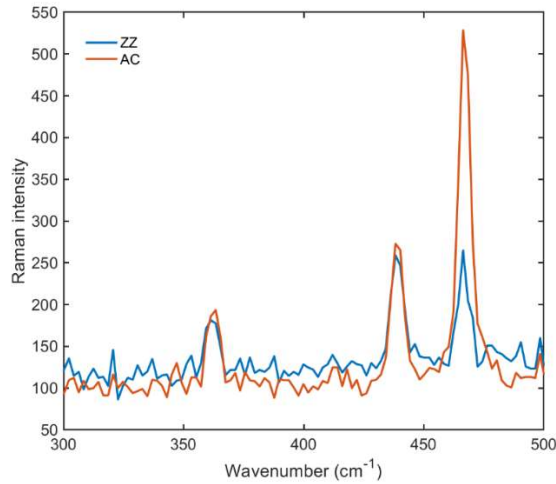


Fig. S2. Polarized Raman spectra measured for the BP device presented in the main manuscript.

Discussion about electro-optic effects at the band edge in BP:

1. *Pauli blocking/Burstein Moss shift.*

The fermionic nature of electrons and holes in a semiconductor dictates that optical transitions between occupied states in the valence band and unoccupied states in the conduction band are blocked if the electron states at the same energy and momentum are already filled, leading to reduced absorption. This effect is known as Pauli blocking/Burstein Moss shift. Additionally, since BP has a quantum well electronic bandstructure, characteristic absorption dips are seen for different subbands as they are filled with increasing doping.

2. *Quantum confined Stark effect.*

When a quantum well is subjected to an external electric field, the electron states shift to lower energies and the hole states to higher energies thereby reducing the effective optical bandgap. Additionally, electrons and holes shift to the opposite sides of the well reducing the overlap integral which reduces the oscillator strength of each transition.

3. *Forbidden transitions /‘mixed’ transitions.*

In an unperturbed quantum well system, certain transitions have allowed dipole transitions and optical matrix elements which do not vanish. From symmetry arguments those transitions happen to be between subbands of equal principal quantum number index ($j=1$ VB to $j=1$ CB, etc.). However, upon the application of an external electric field, modification of the overlap integral between electrons and holes causes the previously vanishing optical transitions to be allowed and they appear as mixed transitions.

4. *Band bending.*

In multilayer systems for a typical field effect heterostructure geometry, a degenerate charge gas is induced at the interface of the active material and the gate dielectric; in our case, the BP/b-hBN interface. However, the charge is not distributed equally in the out of plane direction because the first layer of charge screens the remaining charges. This gives rise to a thickness-dependent charge profile approximated by the Thomas-Fermi screening model. For BP it can be seen from calculations for a charge density of about $5\text{-}7 \times 10^{12}/\text{cm}^2$ the effective channel thickness is about 2.9 nm- meaning the

induced electron/hole gas is two-dimensional in nature and not three-dimensional. In all our fitting routines, it is assumed this is the case, and a sheet conductivity for the 2DEG is used (with a static dielectric constant as a background for the whole BP).

We explain our observation in Figs. 1(H) and (I) (in the main text) as follows. As we dope the system with electrons we see a suppression of absorption along the AC direction (appearing as a dip) due to Pauli blocking which increases with applied voltage. Higher lying features such as subbands show very weak modulation. Additionally, a mild red shift of the band edge is seen at the highest positive voltages indicative of a Stark shift. However, on the hole side, not only do we see a strong dip at the onset of band-edge transition and at the subband energies we also see a stronger red-shift of the band gap due to a more dominant Stark shift. The band-edge shifts to about 2800 cm^{-1} which is $\sim 30\text{ meV}$ below the pristine gap on the hole side, and to about 2900 cm^{-1} which is $\sim 15\text{ meV}$ below the optical gap on the electron side. This asymmetry in the Stark shift might be from impurities/residual doping in the system causing an additional field which cancels out in the electron doped case but adds up in the hole doped case. These impurities could also be causing the reduction of prominent subband oscillations on the electron side. Further nanoscale studies would be needed to elucidate more about the underlying mechanism. The noisy weak modulation for ZZ around 3000 cm^{-1} arises from the fact that the interference dip of the entire stack in our device (which also happens serendipitously to be around the same energy as the band-edge) results in low signal.

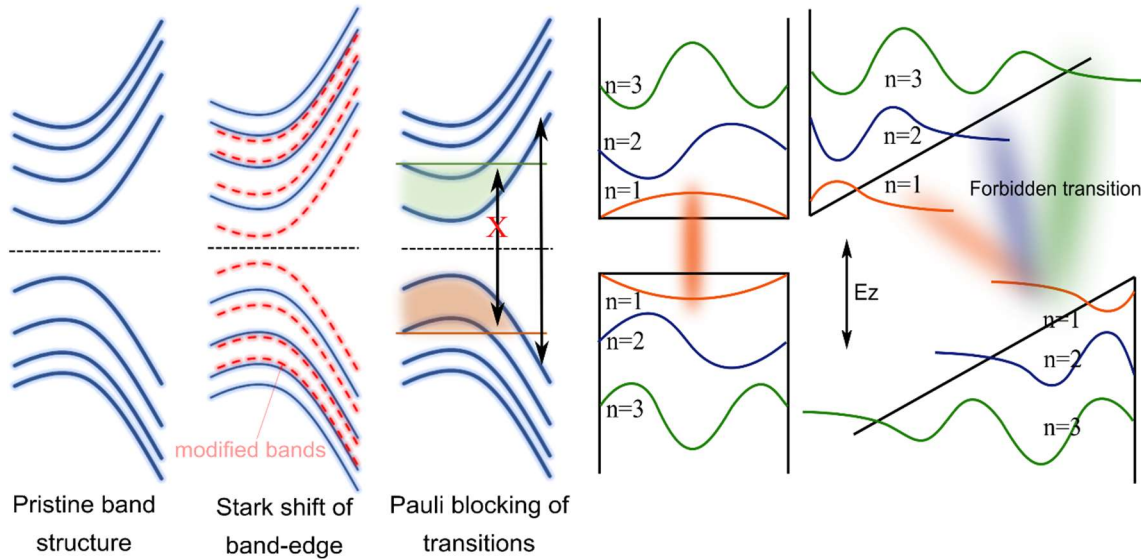


Fig. S3. Quantum Well electro-optic effects. Schematic of different electro-optic effects occurring at energies near and above the band-edge of a multilayer BP thin film.

Unpolarized measurements:

We also repeated measurements on our device without a polarizer and were able to see consistent modulation data both in the interband and the intraband regime. From the fits to the Drude weight, effective

masses that are close to the average of the effective masses of the AC and ZZ axis were obtained, as shown in Fig. S4.

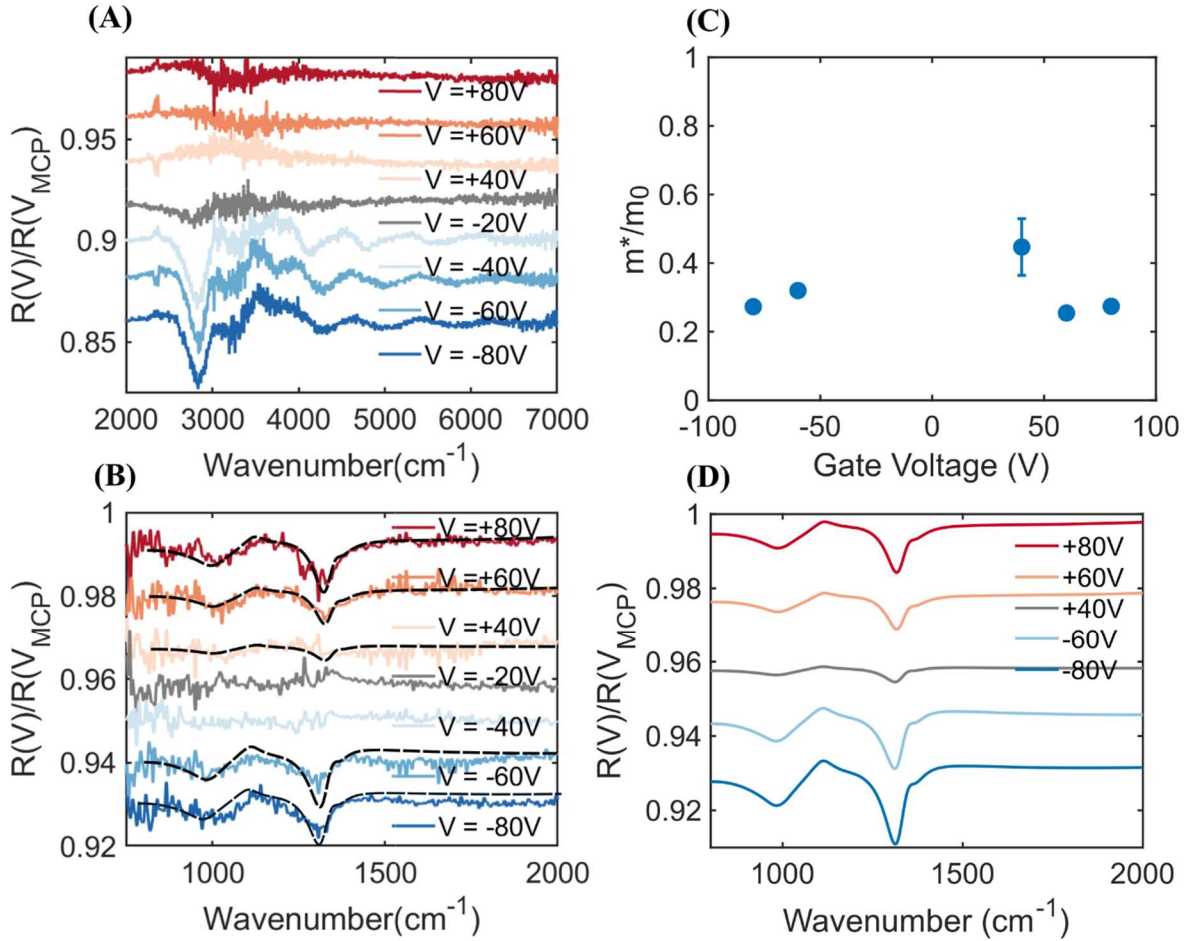


Fig. S4. Unpolarized response from BP device. (A) Unpolarized reflection modulation at the band-edge for different electron and hole densities. (B) Same for below the band-edge region along with fits (dotted black lines). (C) Assuming a parallel plate capacitor model, extracted effective mass of free carriers (D) Fits to the experimental data (some curves at very low voltages [close to MCP] don't fit well due to extremely low signal and have been avoided)

Discussion about the reduction on Drude weights:

From our experiments we are able to extract Drude weights for both polarization (AC and ZZ) and unpolarized light. In order to explain the trends we look carefully at how Drude weight should evolve for a quantum well like system - ($D = \pi e^2 \sum_i n/m_i^*$, $i = \text{subbands}$). Our measured values for the effective mass is slightly higher than that expected for few layer BP. As mentioned in the main text, the origin can be two fold. One can come from the electron confinement. When the doping density is low (near charge neutral), the screening length is $\sim 100\text{nm}$, which means the whole system is uniformly doped and behaves as bulk. However as we dope the system the screening length goes down to $\sim 2\text{-}5\text{nm}$ (most of the charge resides in the first 2-3 layers) and the system becomes highly confined (2D). Previous quantum transport

measurements revealed rather anomalously large average in plane effective masses for BP due to such confinement effects. Another important factor could be the increasing less dispersive nature of the subbands in BP along the AC axis. When we dope the system i.e. increase/decrease its Fermi level we fill up not only the first subband, but also higher subbands. From our reflection modulation data in the interband regime, subband oscillations from the first 4-5 states can be seen, which means the Fermi tail is broad enough to have significant occupation in those states. If we calculate the transition energies based on the thickness of our sample, we find that the subbands are closely spaced. When we then proceed to calculate the effective mass for these subbands (given by $m_x^i = \frac{\hbar^2}{\frac{2\gamma^2}{\delta^i} + \eta}$, where δ^i is the subband energy gap) we see an

increase for higher energy states. It is possible that participation of those fermions leads to an overall increase in the measured effective mass. This can be understood as filling up of the different bands in the system. Since our sample is $\sim 18\text{nm}$ thick, the subbands are placed closely (lying within a few $k_B T$ of each other) and as we gate the heterostructure we move the Fermi level from one subband to the next (also evident from our band edge modulation data). For the ZZ direction any increase can come only from confinement since from theory we don't expect a subband dependent effective mass (given by $m_y^i = \hbar^2/2v_c$). For a more quantitative prediction of how the effective mass evolves, a first-principles theoretical framework would be required which accounts for all the electro-optic effects at work, and this is beyond the scope of the present paper. A table summarizing the possible bounds on effective mass is presented here. The values are based both on our calculations and previous results(28):

Table T1: Bounds on effective masses. The effective masses for electrons and holes in BP can be bounded both due to the screening effect leading to highly confined carriers and also due to different carrier masses coming from higher subbands as the BP is electrostatically gated (i.e. Fermi level is pushed into the conduction or valence subbands). The bounds are presented in this table.

Type of carrier(polarization)	Subband lower bound	Subband higher bound	Confinement lower bound	Confinement higher bound
electron (AC)	0.14m0	0.23m0	0.14m0	0.17m0
electron (ZZ)	-	-	0.71m0	1.16m0
hole (AC)	0.12m0	0.23m0	0.12m0	0.15m0
hole (ZZ)	-	-	0.72m0	1.2m0

The transition energies are calculated from the equation²:

$$\delta_N^n = E_{g0} - 2(\gamma^c - \gamma^v) \cos\left(\frac{n\pi}{N+1}\right)$$

Where E_{g0} is the monolayer optical gap, $\gamma^c(\gamma^v)$ is the nearest neighbor coupling between adjacent layers for conduction (valence band), n is the index of transition, N is the number of layers in the system.

For our case $E_{g0} = 1.82\text{eV}$, $\gamma^c - \gamma^v = 0.73\text{ eV}$. We plot the transition energies and the corresponding calculated effective mass for the AC direction in Fig. S5.

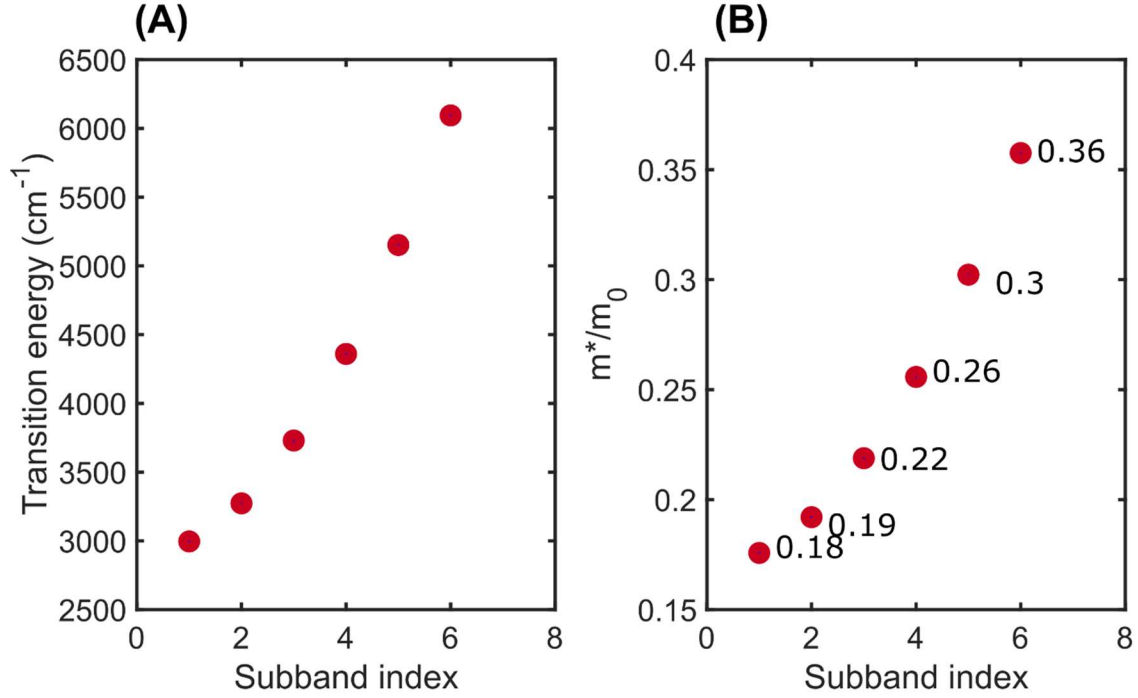


Fig. S5. Subband effect in BP dispersion. (A) Calculation of transition energies in 18.68nm BP. (B) Corresponding effective mass along the Armchair direction.

Transfer matrix model:

We employed a transfer matrix model to account for the multiple reflections in our device. It is formulated as follows –

For a stack consisting of N layers, we have

$$\begin{pmatrix} t \\ 0 \end{pmatrix} = J_{N_{total}} \begin{pmatrix} 1 \\ r \end{pmatrix}, \text{ where } J_{N_{total}} = \prod_{i=1}^N J_i$$

$$J_i = \frac{1}{2} \begin{pmatrix} e^{i(k_i - k_{i+1})z_i} \left(1 + \frac{k_i - \omega\mu_0\sigma}{k_{i+1}} \right) & e^{-i(k_i + k_{i+1})z_i} \left(1 - \frac{k_i + \omega\mu_0\sigma}{k_{i+1}} \right) \\ e^{i(k_i + k_{i+1})z_i} \left(1 - \frac{k_i - \omega\mu_0\sigma}{k_{i+1}} \right) & e^{-i(k_i - k_{i+1})z_i} \left(1 + \frac{k_i + \omega\mu_0\sigma}{k_{i+1}} \right) \end{pmatrix},$$

$k = \text{wavevector}, z = \text{thickness}, i = \text{layer index}$

The term $\omega\mu_0\sigma$ is invoked only at interfaces containing the 2DEG, else excluded.

Reflection and transmission is given by :

$$T = \frac{\tilde{n}_N}{\tilde{n}_1} |t|^2, \quad R = |r|^2, \quad \text{where } \tilde{n}_m = \text{complex refractive index of layer } - m$$

The complex permittivity of SiO₂ is adopted from Kischkat et al. shown in Fig. S6, and that of Si is adopted from Salzberg et al (61-63). The permittivity of hBN is modelled using a single Lorentzian oscillator (we only probe the in-plane phonon since the incident E-field is perpendicular to the c-axis), extracted by fitting the reflection data near the hBN phonon.

$$\epsilon_{hBN} = \frac{\epsilon_{\infty}(1 + \omega_{pl}^2)}{\omega_{tl}^2 - \omega^2 - i\gamma\omega}$$

$$\epsilon_{hBN} = 4.95, \omega_{pl} = 841.25 \text{ cm}^{-1}, \omega_{tl} = 1368.4 \text{ cm}^{-1}, \gamma = 9.42 \text{ cm}^{-1} \quad (\text{top hBN})$$

$$\epsilon_{hBN} = 4.95, \omega_{pl} = 850.12 \text{ cm}^{-1}, \omega_{tl} = 1364.1 \text{ cm}^{-1}, \gamma = 9.31 \text{ cm}^{-1} \quad (\text{bottom hBN})$$

The 2DEG formed simultaneously of opposite charge in the Si is modelled as : $\sigma = \frac{n_{Si}e^2m_{eff}^{-1}}{\omega+i\Gamma}$, where n_{Si} is equal to n_{BP} , $m_{eff} = 0.26m_0$ (for electrons), $0.386m_0$ (for holes), $\Gamma=130\text{cm}^{-1}$.

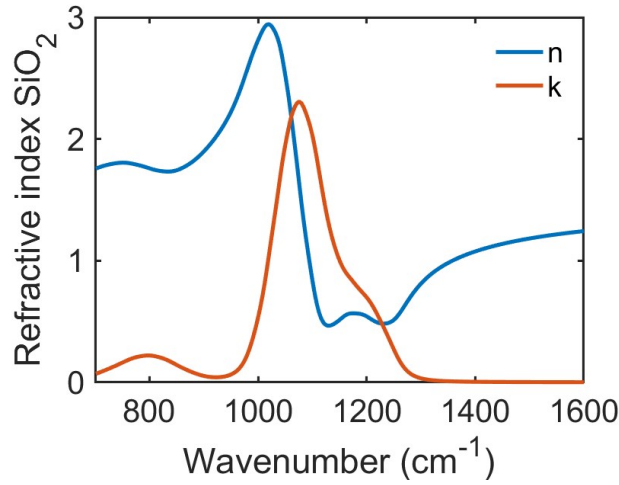


Fig. S6. SiO₂ refractive index. n,k data adopted for SiO₂ (dominated by phonons).

Modulation line shape:

The observed modulation line shapes below the band edge are reminiscent of Fano-like resonances in our measurements. A Fano resonance occurs when there is an optical coupling between a sharp resonance like a narrow linewidth phonon and a broad continuum like the intraband Drude absorption in BP. We neglect the effect of Si 2DEG to simplify our analysis (it behaves similar to the BP 2DEG except the anisotropy). We examine the Fano lineshape in the presence of each phonon system (namely, hBN and SiO₂) with BP in Fig. S7. For hBN a sharp phonon dominates the Fano resonance; however for SiO₂ several phonons contribute to the Fano resonance. Overall, we see a superposition of these resonances in the experimental data, since both materials are present in our heterostructures. For clarity, the charge density in BP was assumed to be $10^{13}/\text{cm}^2$ with the polarization along the AC direction.

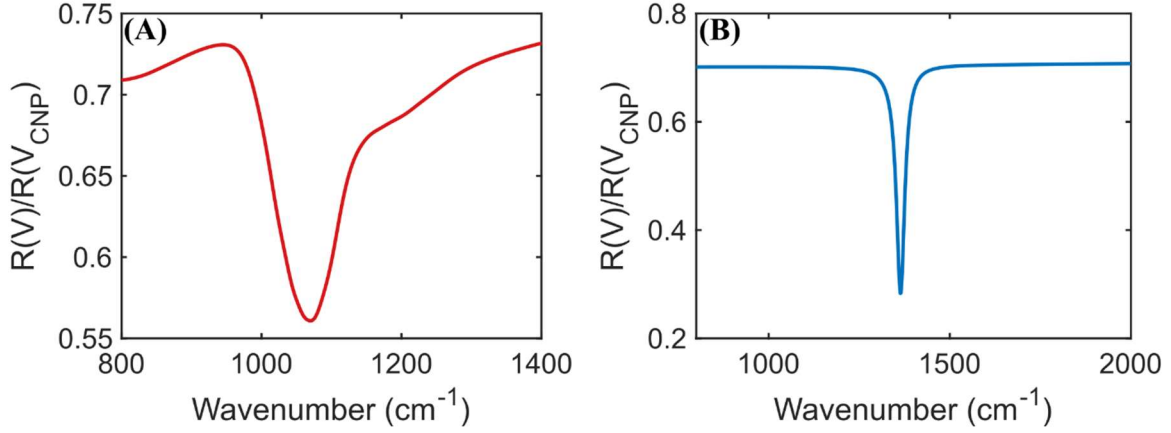


Fig. S7. Fano response in the system. (A) Fano like response for BP/SiO₂ system. **(B)** Same for BP/hBN system.

Refractive index and optical conductivity for BP 2DEG:

In order to account for screening, we model the BP as two parts – 1. An actively electronically modulated 2DEG (thickness extracted from Thomas-Fermi screening calculations done in S13) and 2. A non-modulated bulk region. It is schematically shown in Fig. S8.

We also extract refractive index (n, k) data for the modulated 2DEG (with an assumed thickness of 2.9nm) from the obtained σ and plot them in Fig. S9 and S10, respectively. The static contribution to the anisotropic dielectric function is modelled by using contribution from higher energy oscillators, taken from bulk BP studies, previously shown to be a reasonable approximation for other two-dimensional systems. The results have been extrapolated to much lower photon energies for clarity since the Drude model is expected to suffice. Here, $\sigma_0 = \frac{e^2}{4\hbar}$.

The following relations are employed –

$$\epsilon_{jj}(\omega) = \epsilon_{\infty} + \frac{i\sigma(\omega)}{t\epsilon_0\omega}, \tilde{n}(\omega) = \sqrt{\epsilon_{jj}(\omega)}, \text{ where } t = \text{thickness of the 2DEG}$$

$$\epsilon_{\infty}(\text{AC/ZZ}) = 12.5/10.2$$

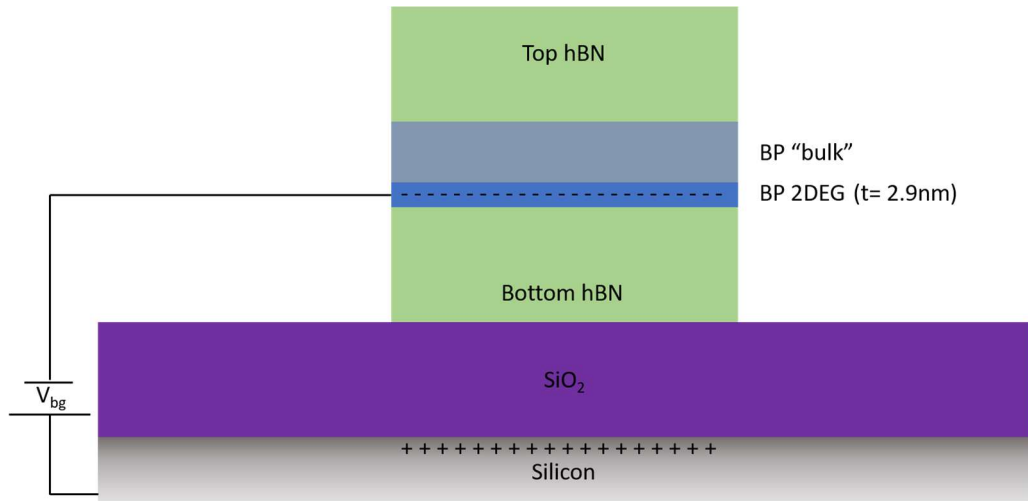


Figure S8. Schematic of electrostatic gating in BP device. The formation of an inversion layer is indicated at the interface of SiO₂/Si and bottom hBN/BP (of opposite parity). The BP can be modelled as two separate parts – 1. Actively electronically modulated labeled as “BP 2DEG” which is ~2.9 nm thick from Thomas-Fermi screening calculations and 2. A non-modulated thick region labeled as “BP bulk” which extends to the remainder of the physical thickness of the BP flake as measured by atomic force microscopy (AFM).

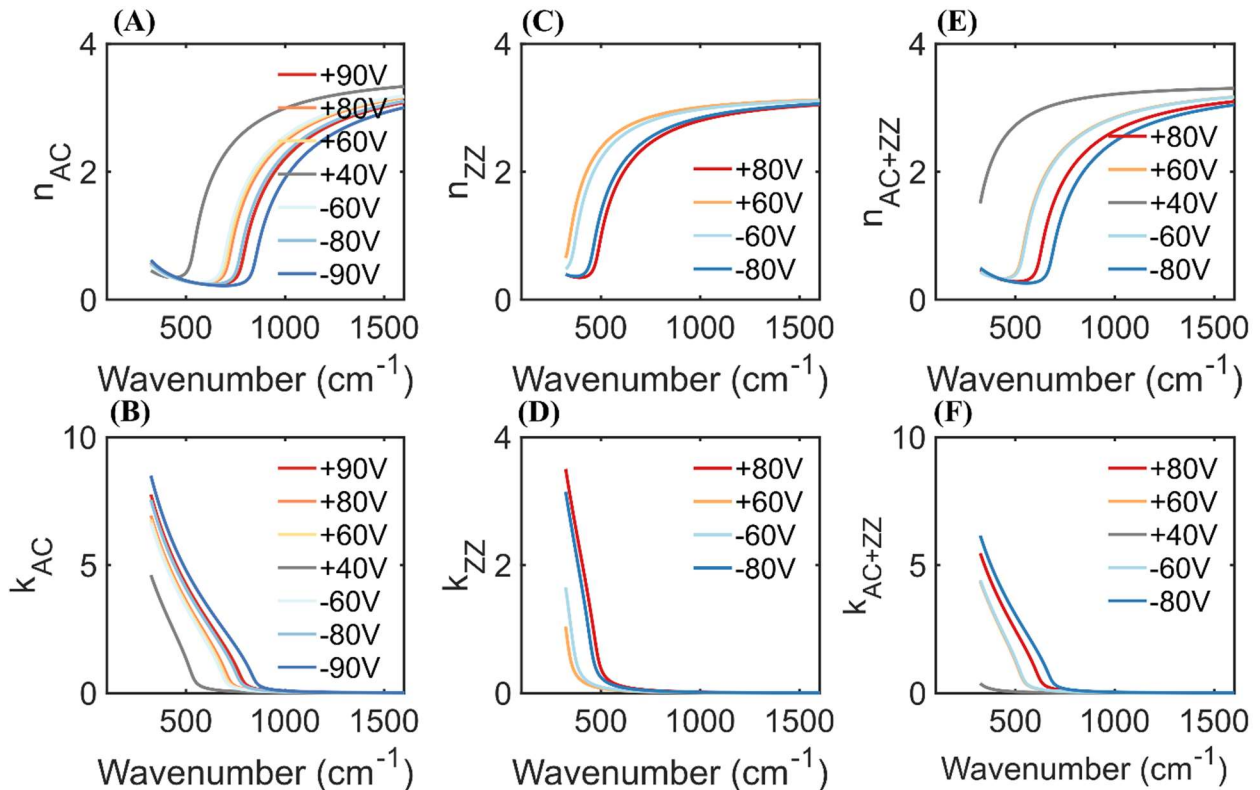


Fig. S9. Refractive index of doped BP. (A) Extracted real part of refractive index of BP 2DEG as a function of voltage for AC excitation. (B) Extracted imaginary part of refractive index of BP 2DEG as a

function of voltage for AC excitation. (C),(D) Same as (A),(B) but for ZZ excitation. (E),(F) Same as (A),(B) but for unpolarized excitation.

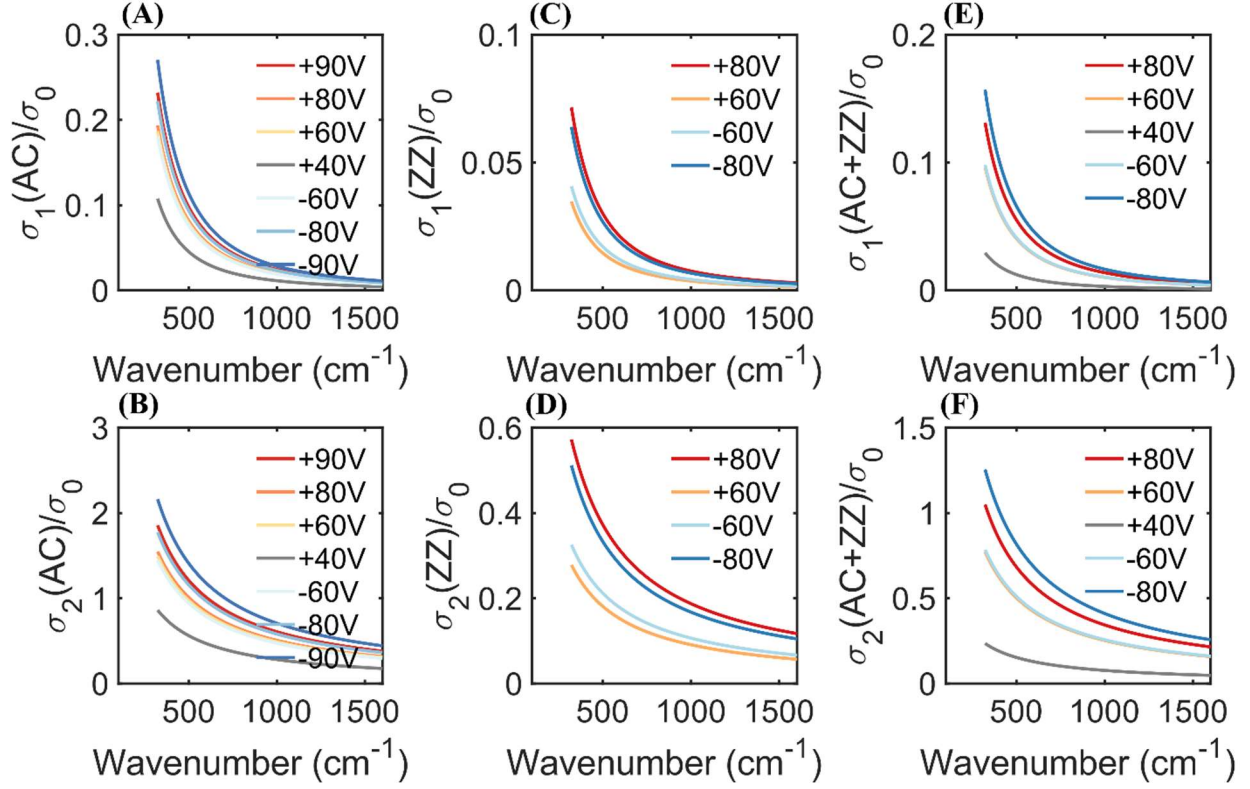


Fig. S10. Optical conductivity of doped BP. (A) Extracted real part of optical conductivity of BP 2DEG as a function of voltage for AC excitation. (B) Extracted imaginary part of optical conductivity of BP 2DEG as a function of voltage for AC excitation. (C),(D) Same as (A),(B) but for ZZ excitation. (E),(F) Same as (A),(B) but for unpolarized excitation. Here, $\sigma_0 = \frac{e^2}{4\hbar}$.

AFM data:

AFM scans to measure the thickness of BP, and top and bottom hBN flakes are shown in Fig. S11

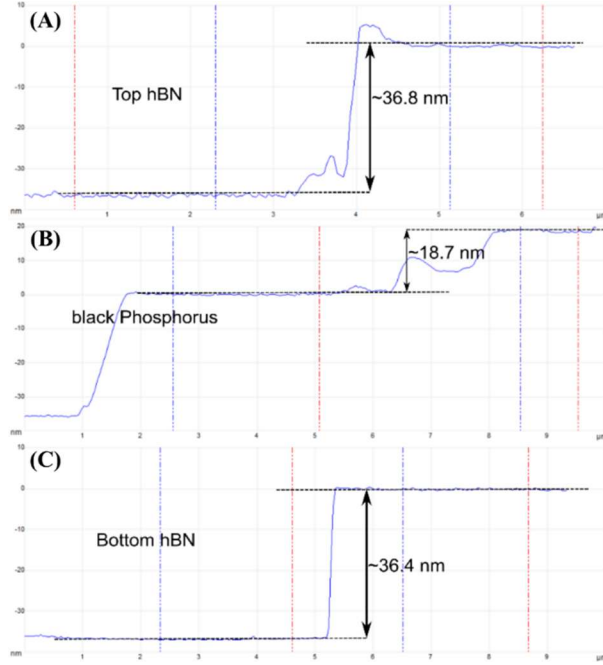


Fig. S11. AFM data. (A) AFM line scan for top hBN. (B) AFM line scan for BP flake. (C) AFM line scan for bottom hBN.

Parallel plate capacitor model:

The electrostatics of our device is modelled as follows – the voltage applied between BP and the Si causes the hBN and SiO₂ to act as a dielectric between two parallel plates (BP and Si). The capacitance is calculated as :

$$C_i = \frac{\epsilon_0 \epsilon_{r,i} A}{d}, i - \text{denotes the material (hBN and SiO}_2\text{)}$$

hBN and SiO₂ are in series, so the capacitance adds up as $C_{eff} = \frac{C_1 C_2}{C_1 + C_2}$. Assuming $\epsilon=3.9$ for both hBN and SiO₂, we obtain $C_{eff}=10.7nF/cm^2$. Plugging this into $q = C * (V - V_{MCP})$, we get the charge density in the induced gas in BP ($V_{MCP} = 17V$), as plotted in Fig. S12. At the highest voltages on the electron side we induce upto $4.9 \times 10^{12}/cm^2$, and on the hole side we induce upto $7.2 \times 10^{12}/cm^2$. Even higher charge density may be had by going to higher voltages, however to be able to reliably repeat measurements on the same device without any breakdown, such regimes were avoided.

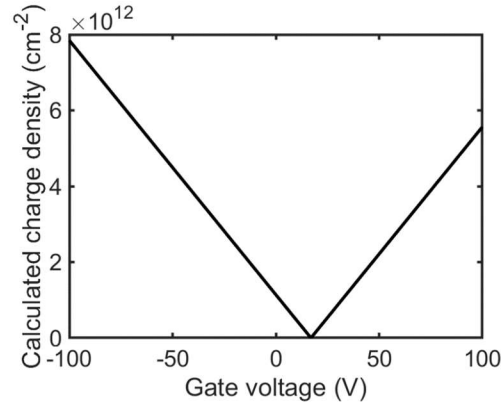


Fig. S12. Capacitor model for BP. Charge density induced in BP as calculated from parallel plate capacitor model.

Thomas Fermi screening model:

The charge induced in BP is not uniformly spread over the entire thickness, rather concentrated in the first 2-3 layers and then decaying exponentially. A Thomas-Fermi screening model is employed to understand the charge distribution in BP, shown in Fig. S13. A length scale of ~ 2.9 nm for a charge density of about $5-7 \times 10^{12}/\text{cm}^2$ is obtained for the effective thickness of the 2DEG, which is then used to calculate the dielectric constant and the refractive index.

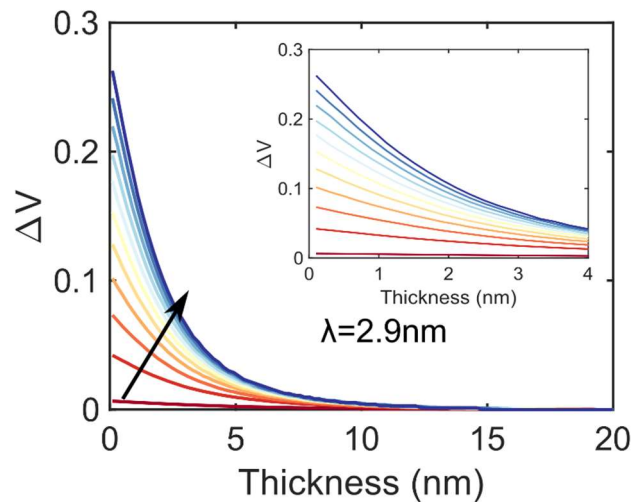


Fig. S13. Band-bending in BP. Thomas Fermi screening calculation in BP as the charge density varies from $10^{11}/\text{cm}^2$ to $10^{13}/\text{cm}^2$. Inset – zoomed in upto 4 nm.

Dirac- plasmonic point :

We note that for the carrier densities obtained in the measurements there exists a Dirac-plasmonic point (DPP) where the isofrequency contour dispersion almost becomes linear. However, this happens at frequencies slightly below the cutoff of our measurements. The DPP is quite sensitive to the doping and also the frequency as summarized in Fig. S14.

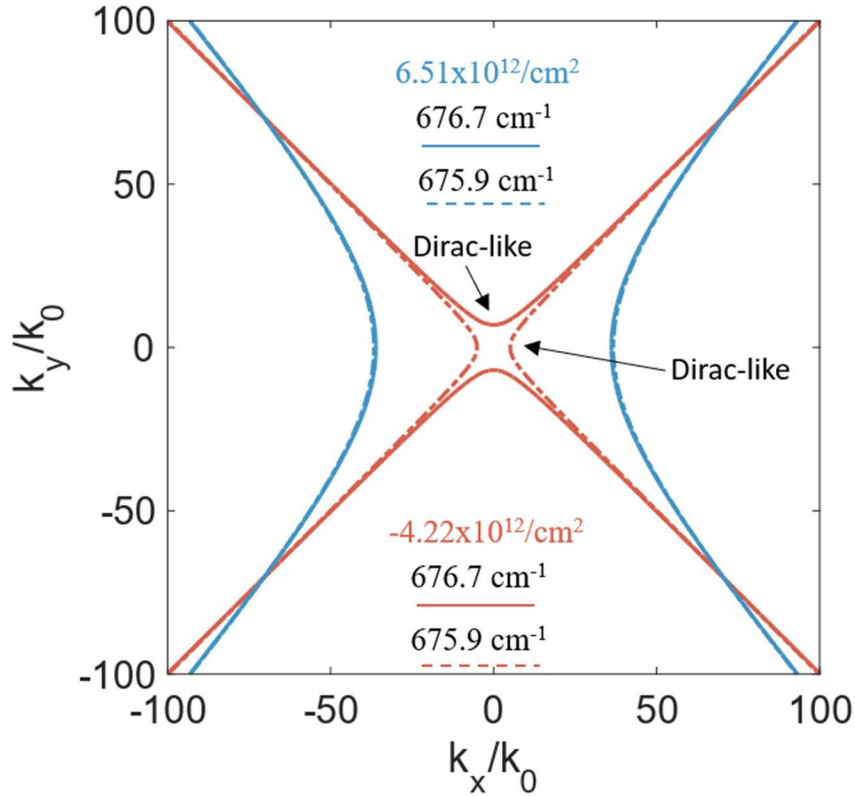


Fig. S14. Isofrequency contours (IFC) around Dirac-plasmonic point. IFCs are calculated for in-plane propagating plasmon (TM) modes at two frequencies – 676.7 cm^{-1} and 659.9 cm^{-1} and two carrier densities – $4.22 \times 10^{12}/\text{cm}^2$ (electron) and $6.51 \times 10^{12}/\text{cm}^2$ (hole). For higher doping densities the IFCs are less sensitive to small changes in the frequency, however for lower doping densities the IFCs are quite sensitive to small changes in the frequency and flip the sign of the hyperbolic dispersion. They also become almost linear adopting a Dirac-like nature.

REFERENCES AND NOTES

1. A. Poddubny, I. Iorsh, P. Belov, Y. Kivshar, Hyperbolic metamaterials. *Nat. Photonics* **7**, 958–967 (2013).
2. H. N. S. Krishnamoorthy, Z. Jacob, E. Narimanov, I. Kretzschmar, V. M. Menon, Topological transitions in metamaterials. *Science* **336**, 205–209 (2012).
3. D. Lu, J. J. Kan, E. E. Fullerton, Z. Liu, Enhancing spontaneous emission rates of molecules using nanopatterned multilayer hyperbolic metamaterials. *Nat. Nanotechnol.* **9**, 48–53 (2014).
4. A. A. High, R. C. Devlin, A. Dibos, M. Polking, D. S. Wild, J. Perczel, N. P. de Leon, M. D. Lukin, H. Park, Visible-frequency hyperbolic metasurface. *Nature* **522**, 192–196 (2015).
5. Z. Liu, H. Lee, Y. Xiong, C. Sun, X. Zhang, Far-field optical hyperlens magnifying sub-diffraction-limited objects. *Science* **315**, 1686 (2007).
6. S.-A. Biehs, M. Tschikin, R. Messina, P. Ben-Abdallah, Super-Planckian near-field thermal emission with phonon-polaritonic hyperbolic metamaterials. *Appl. Phys. Lett.* **102**, 131106 (2013).
7. J. D. Caldwell, A. V. Kretinin, Y. Chen, V. Giannini, M. M. Fogler, Y. Francescato, C. T. Ellis, J. G. Tischler, C. R. Woods, A. J. Giles, M. Hong, K. Watanabe, T. Taniguchi, S. A. Maier, K. S. Novoselov, Sub-diffractive volume-confined polaritons in the natural hyperbolic material hexagonal boron nitride. *Nat. Commun.* **5**, 5221 (2014).
8. D. Correas-Serrano, J. S. Gomez-Diaz, A. A. Melcon, A. Alù, Black phosphorus plasmonics: Anisotropic elliptical propagation and nonlocality-induced canalization. *J. Optics* **18**, 104006 (2016).
9. A. Alù, M. G. Silveirinha, A. Salandrino, N. Engheta, Epsilon-near-zero metamaterials and electromagnetic sources: Tailoring the radiation phase pattern. *Phys. Rev. B.* **75**, 155410 (2007).
10. M. Silveirinha, N. Engheta, Tunneling of electromagnetic energy through subwavelength channels and bends using ϵ -near-zero materials. *Phys. Rev. Lett.* **97**, 157403 (2006).

11. T. Xu, H. J. Lezec, Visible-frequency asymmetric transmission devices incorporating a hyperbolic metamaterial. *Nat. Commun.* **5**, 4141 (2014).
12. C. Wang, S. Huang, Q. Xing, Y. Xie, C. Song, F. Wang, H. Yan, Van der Waals thin films of WTe₂ for natural hyperbolic plasmonic surfaces. *Nat. Commun.* **11**, 1158 (2020).
13. S. Dai, Z. Fei, Q. Ma, A. S. Rodin, M. Wagner, A. S. McLeod, M. K. Liu, W. Gannett, W. Regan, K. Watanabe, T. Taniguchi, M. Thiemens, G. Dominguez, A. H. C. Neto, A. Zettl, F. Keilmann, P. Jarillo-Herrero, M. M. Fogler, D. N. Basov, Tunable phonon polaritons in atomically thin van der Waals crystals of boron nitride. *Science* **343**, 1125–1129 (2014).
14. J. Sun, J. Zhou, B. Li, F. Kang, Indefinite permittivity and negative refraction in natural material: Graphite. *Appl. Phys. Lett.* **98**, 101901 (2011).
15. G. X. Ni, A. S. McLeod, Z. Sun, L. Wang, L. Xiong, K. W. Post, S. S. Sunku, B.-Y. Jiang, J. Hone, C. R. Dean, M. M. Fogler, D. N. Basov, Fundamental limits to graphene plasmonics. *Nature* **557**, 530–533 (2018).
16. L. Ju, B. Geng, J. Horng, C. Girit, M. Martin, Z. Hao, H. A. Bechtel, X. Liang, A. Zettl, Y. R. Shen, F. Wang, Graphene plasmonics for tunable terahertz metamaterials. *Nat. Nanotechnol.* **6**, 630–634 (2011).
17. Z. Fei, A. S. Rodin, G. O. Andreev, W. Bao, A. S. McLeod, M. Wagner, L. M. Zhang, Z. Zhao, M. Thiemens, G. Dominguez, M. M. Fogler, A. H. C. Neto, C. N. Lau, F. Keilmann, D. N. Basov, Gate-tuning of graphene plasmons revealed by infrared nano-imaging. *Nature* **486**, 82–85 (2012).
18. J. Chen, M. Badioli, P. Alonso-González, S. Thongrattanasiri, F. Huth, J. Osmond, M. Spasenović, A. Centeno, A. Pesquera, P. Godignon, A. Z. Elorza, N. Camara, F. J. G. de Abajo, R. Hillenbrand, F. H. L. Koppens, Optical nano-imaging of gate-tunable graphene plasmons. *Nature* **487**, 77–81 (2012).
19. K. v. Klitzing, G. Dorda, M. Pepper, New method for high-accuracy determination of the fine-structure constant based on quantized hall resistance. *Phys. Rev. Lett.* **45**, 494–497 (1980).

20. B. Jeckelmann, B. Jeanneret, The quantum Hall effect as an electrical resistance standard. *Rep. Prog. Phys.* **64**, 1603 (2001).
21. M. Liu, X. Yin, E. Ulin-Avila, B. Geng, T. Zentgraf, L. Ju, F. Wang, X. Zhang, A graphene-based broadband optical modulator. *Nature* **474**, 64–67 (2011).
22. M. Liu, X. Yin, X. Zhang, Double-layer graphene optical modulator. *Nano Lett.* **12**, 1482–1485 (2012).
23. B. Sensale-Rodriguez, R. Yan, M. M. Kelly, T. Fang, K. Tahy, W. S. Hwang, D. Jena, L. Liu, H. G. Xing, Broadband graphene terahertz modulators enabled by intraband transitions. *Nat. Commun.* **3**, 780 (2012).
24. G. Long, D. Maryenko, J. Shen, S. Xu, J. Hou, Z. Wu, W. K. Wong, T. Han, J. Lin, Y. Cai, R. Lortz, N. Wang, Achieving ultrahigh carrier mobility in two-dimensional hole gas of black phosphorus. *Nano Lett.* **16**, 7768–7773 (2016).
25. N. Gillgren, D. Wickramaratne, Y. Shi, T. Espiritu, J. Yang, J. Hu, J. Wei, X. Liu, Z. Mao, K. Watanabe, T. Taniguchi, M. Bockrath, Y. Barlas, R. K. Lake, C. N. Lau, Gate tunable quantum oscillations in air-stable and high mobility few-layer phosphorene heterostructures. *2D Mater.* **2**, 011001 (2014).
26. X. Chen, Y. Wu, Z. Wu, Y. Han, S. Xu, L. Wang, W. Ye, T. Han, Y. He, Y. Cai, N. Wang, High-quality sandwiched black phosphorus heterostructure and its quantum oscillations. *Nat. Commun.* **6**, 7315 (2015).
27. L. Li, Y. Yu, G. J. Ye, Q. Ge, X. Ou, H. Wu, D. Feng, X. H. Chen, Y. Zhang, Black phosphorus field-effect transistors. *Nat. Nanotechnol.* **9**, 372–377 (2014).
28. L. Li, G. J. Ye, V. Tran, R. Fei, G. Chen, H. Wang, J. Wang, K. Watanabe, T. Taniguchi, L. Yang, X. H. Chen, Y. Zhang, Quantum oscillations in a two-dimensional electron gas in black phosphorus thin films. *Nat. Nanotechnol.* **10**, 608–613 (2015).

29. L. Li, F. Yang, G. J. Ye, Z. Zhang, Z. Zhu, W. Lou, X. Zhou, L. Li, K. Watanabe, T. Taniguchi, K. Chang, Y. Wang, X. H. Chen, Y. Zhang, Quantum Hall effect in black phosphorus two-dimensional electron system. *Nat. Nanotechnol.* **11**, 593–597 (2016).
30. C. A. Valagiannopoulos, M. Mattheakis, S. N. Shirodkar, E. Kaxiras, Manipulating polarized light with a planar slab of black phosphorus. *J. Phys. Commun.* **1**, 45003 (2017).
31. A. Castellanos-Gomez, L. Vicarelli, E. Prada, J. O. Island, K. L. Narasimha-Acharya, S. I. Blanter, D. J. Groenendijk, M. Buscema, G. A. Steele, J. V. Alvarez, H. W. Zandbergen, J. J. Palacios, H. S. J. van der Zant, Isolation and characterization of few-layer black phosphorus. *2D Mater.* **1**, 025001 (2014).
32. V. Tran, R. Soklaski, Y. Liang, L. Yang, Layer-controlled band gap and anisotropic excitons in few-layer black phosphorus. *Phys. Rev. B.* **89**, 235319 (2014).
33. D. Y. Qiu, F. H. da Jornada, S. G. Louie, Environmental screening effects in 2D materials: Renormalization of the bandgap, electronic structure, and optical spectra of few-layer black phosphorus. *Nano Lett.* **17**, 4706–4712 (2017).
34. G. Zhang, S. Huang, F. Wang, Q. Xing, C. Song, C. Wang, Y. Lei, M. Huang, H. Yan, The optical conductivity of few-layer black phosphorus by infrared spectroscopy. *Nat. Commun.* **11**, 1847 (2020).
35. R. Xu, S. Zhang, F. Wang, J. Yang, Z. Wang, J. Pei, Y. W. Myint, B. Xing, Z. Yu, L. Fu, Q. Qin, Y. Lu, Extraordinarily bound quasi-one-dimensional trions in two-dimensional phosphorene atomic semiconductors. *ACS Nano* **10**, 2046–2053 (2016).
36. A. Chaves, T. Low, P. Avouris, D. Çakır, F. M. Peeters, Anisotropic exciton Stark shift in black phosphorus. *Phys. Rev. B.* **91**, 155311 (2015).
37. X. Zhou, W.-K. Lou, F. Zhai, K. Chang, Anomalous magneto-optical response of black phosphorus thin films. *Phys. Rev. B.* **92**, 165405 (2015).

38. S. Huang, G. Zhang, F. Fan, C. Song, F. Wang, Q. Xing, C. Wang, H. Wu, H. Yan, Strain-tunable van der Waals interactions in few-layer black phosphorus. *Nat. Commun.* **10**, 2447 (2019).
39. J. Quereda, P. San-Jose, V. Parente, L. Vaquero-Garzon, A. J. Molina-Mendoza, N. Agrait, G. Rubio-Bollinger, F. Guinea, R. Roldán, A. Castellanos-Gomez, Strong modulation of optical properties in black phosphorus through strain-engineered rippling. *Nano Lett.* **16**, 2931–2937 (2016).
40. G. Zhang, A. Chaves, S. Huang, F. Wang, Q. Xing, T. Low, H. Yan, Determination of layer-dependent exciton binding energies in few-layer black phosphorus. *Sci. Adv.* **4**, eaap9977 (2018).
41. L. Li, J. Kim, C. Jin, G. J. Ye, D. Y. Qiu, F. H. da Jornada, Z. Shi, L. Chen, Z. Zhang, F. Yang, K. Watanabe, T. Taniguchi, W. Ren, S. G. Louie, X. H. Chen, Y. Zhang, F. Wang, Direct observation of the layer-dependent electronic structure in phosphorene. *Nat. Nanotechnol.* **12**, 21–25 (2017).
42. C. Lin, R. Grassi, T. Low, A. S. Helmy, Multilayer black phosphorus as a versatile mid-infrared electro-optic material. *Nano Lett.* **16**, 1683–1689 (2016).
43. W. S. Whitney, M. C. Sherrott, D. Jariwala, W.-H. Lin, H. A. Bechtel, G. R. Rossman, H. A. Atwater, Field effect optoelectronic modulation of quantum-confined carriers in black phosphorus. *Nano Lett.* **17**, 78–84 (2020).
44. M. C. Sherrott, W. S. Whitney, D. Jariwala, S. Biswas, C. M. Went, J. Wong, G. R. Rossman, H. A. Atwater, Anisotropic quantum well electro-optics in few-layer black phosphorus. *Nano Lett.* **19**, 269–276 (2019).
45. C. Chen, X. Lu, B. Deng, X. Chen, Q. Guo, C. Li, C. Ma, S. Yuan, E. Sung, K. Watanabe, T. Taniguchi, L. Yang, F. Xia, Widely tunable mid-infrared light emission in thin-film black phosphorus. *Sci. Adv.* **6**, eaay6134 (2020).
46. R. Peng, K. Khaliji, N. Youngblood, R. Grassi, T. Low, M. Li, Midinfrared electro-optic modulation in few-layer black phosphorus. *Nano Lett.* **17**, 6315–6320 (2017).
47. T. Low, A. S. Rodin, A. Carvalho, Y. Jiang, H. Wang, F. Xia, A. H. Castro Neto, Tunable optical properties of multilayer black phosphorus thin films. *Phys. Rev. B.* **90**, 075434 (2014).

48. T. Low, R. Roldán, H. Wang, F. Xia, P. Avouris, L. M. Moreno, F. Guinea, Plasmons and screening in monolayer and multilayer black phosphorus. *Phys. Rev. Lett.* **113**, 106802 (2014).
49. Y.-C. Chang, C.-H. Liu, C.-H. Liu, S. Zhang, S. R. Marder, E. E. Narimanov, Z. Zhong, T. B. Norris, Realization of mid-infrared graphene hyperbolic metamaterials. *Nat. Commun.* **7**, 10568 (2016).
50. J. S. Gomez-Diaz, M. Tymchenko, A. Alù, Hyperbolic plasmons and topological transitions over uniaxial metasurfaces. *Phys. Rev. Lett.* **114**, 233901 (2015).
51. H. Asahina, A. Morita, Band structure and optical properties of black phosphorus. *J. Phys. C: Solid State Phys.* **17**, 1839 (1984).
52. P. Fan, Z. Yu, S. Fan, M. L. Brongersma, Optical Fano resonance of an individual semiconductor nanostructure. *Nat. Mater.* **13**, 471–475 (2014).
53. B. Luk'yanchuk, N. I. Zheludev, S. A. Maier, N. J. Halas, P. Nordlander, H. Giessen, C. T. Chong, The Fano resonance in plasmonic nanostructures and metamaterials. *Nat. Mater.* **9**, 707–715 (2010).
54. B. Scharf, V. Perebeinos, J. Fabian, P. Avouris, Effects of optical and surface polar phonons on the optical conductivity of doped graphene. *Phys. Rev. B.* **87**, 035414 (2013).
55. A. Principi, M. Carrega, M. B. Lundeberg, A. Woessner, F. H. L. Koppens, G. Vignale, M. Polini, Plasmon losses due to electron-phonon scattering: The case of graphene encapsulated in hexagonal boron nitride. *Phys. Rev. B.* **90**, 165408 (2014).
56. Z. Fei, G. O. Andreev, W. Bao, L. M. Zhang, A. S. McLeod, C. Wang, M. K. Stewart, Z. Zhao, G. Dominguez, M. Thiemens, M. M. Fogler, M. J. Tauber, A. H. Castro-Neto, C. N. Lau, F. Keilmann, D. N. Basov, Infrared nanoscopy of dirac plasmons at the graphene-SiO₂ interface. *Nano Lett.* **11**, 4701–4705 (2011).
57. M. Mattheakis, C. A. Valagiannopoulos, E. Kaxiras, Epsilon-near-zero behavior from plasmonic Dirac point: Theory and realization using two-dimensional materials. *Phys. Rev. B.* **94**, 201404 (2016).

58. A. Raja, L. Waldecker, J. Zipfel, Y. Cho, S. Brem, J. D. Ziegler, M. Kulig, T. Taniguchi, K. Watanabe, E. Malic, T. F. Heinz, T. C. Berkelbach, A. Chernikov, Dielectric disorder in two-dimensional materials. *Nat. Nanotechnol.* **14**, 832–837 (2019).
59. J. González, F. Guinea, M. A. H. Vozmediano, Unconventional quasiparticle lifetime in graphite. *Phys. Rev. Lett.* **77**, 3589–3592 (1996).
60. Y. Liu, P. P. Ruden, Temperature-dependent anisotropic charge-carrier mobility limited by ionized impurity scattering in thin-layer black phosphorus. *Phys. Rev. B.* **95**, 165446 (2017).
61. J. Kischkat, S. Peters, B. Gruska, M. Semtsiv, M. Chashnikova, M. Klinkmüller, O. Fedosenko, S. Machulik, A. Aleksandrova, G. Monastyrskyi, Y. Flores, W. Ted Masselink, Mid-infrared optical properties of thin films of aluminum oxide, titanium dioxide, silicon dioxide, aluminum nitride, and silicon nitride. *Appl. Optics* **51**, 6789–6798 (2012).
62. B. Tatian, Fitting refractive-index data with the Sellmeier dispersion formula. *Appl. Optics* **23**, 4477–4485 (1984).
63. C. D. Salzberg, J. J. Villa, Infrared refractive indexes of silicon germanium and modified selenium glass. *J. Opt. Soc. Am.* **47**, 244–246 (1957).